Research Article

Journal of Environmental Nanotechnology

Development of an In_2O_3/g-C_3N_4 Chemiresistive Sensor for Machine Learning-Assisted Discrimination of Acetone and Ethanol Vapors

R. Gowrishankar[1], K. Malarkodi[2*], M. Saravanan[3], V. Rajesh[4], Kudumu Kavitha[5] and Surrya Prakash Dillibabu[6]

[1]Department of Electronics and Communication Engineering, KIT-Kalaignarkarunanidhi Institute of Technology, Coimbatore, TN, India
[2]Department of Master of Business Administration, M. Kumarasamy College of Engineering, Thalavapalayam, Karur, TN, India
[3]Department of Electronics and Communication Engineering, Annamalai University, Faculty of Engineering and Technology, Annamalainagar, Chidambaram, Cuddalore, TN, India
[4]Department of Electronics and Communication Engineering, Koneru Lakshmaiah Education Foundation, Guntur, AP, India
[5]Department of Computer Applications, Madanapalle Institute of Technology and Science (MITS) Deemed to be University, Madanapalle, AP, India
[6]Department of Mechanical Engineering, Vel Tech Rangarajan Dr. Sagunthala R&D Institute of Science and Technology, Chennai, TN, India
Received: 04.07.2026 Accepted: 05.08.2026 Published: xx.xx.xxxx
*kmnimu@gmail.com

ABSTRACT

Differentiating volatile organic vapors, particularly acetone and ethanol remains a persistent limitation for metal oxide chemiresistive sensing devices. This investigation addresses the challenge by integrating the gas-sensing characteristics of In_2O_3/g-C_3N_4 (Indium Oxide/Graphitic Carbon Nitride) with advanced machine learning (ML) methods. The study encompasses the fabrication, physicochemical characterization, and sensing assessment of In_2O_3/g-C_3N_4 nanostructures toward ethanol and acetone vapors. Gas-sensing measurements performed over concentrations of 250–1000 ppm and operating temperatures between 210 and 300 °C revealed only marginal distinction between the two analytes. To improve their differentiation, the recorded transient sensing profiles were interpreted through the Langmuir–Hinshelwood kinetic model, providing microscopic insight into the surface reaction mechanism. The calculated activation energies were 0.28 eV for ethanol and 0.37 eV for acetone, indicating that ethanol undergoes surface interaction more readily, resulting in a comparatively stronger sensing signal. In addition, Support Vector Machine (SVM), Extreme Gradient Boosting (XGBoost), Artificial Neural Network (ANN), Random Forest (RF), and Light Gradient Boosting Machine (LightGBM) models were applied to the experimental sensing dataset to enable dependable identification and separation of ethanol and acetone vapors, with the ANN model demonstrating the highest classification performance, followed by RF, LightGBM, XGBoost, and SVM.

Keywords: Chemiresistive sensing; Machine learning; Kinetic model; Acetone; Ethanol; Gas sensing.

1. INTRODUCTION

Volatile organic compounds (VOCs), particularly ethanol and acetone are hazardous pollutants widely emitted from industrial and biomedical processes. Their similar molecular structures often result in poor gas discrimination, highlighting the need for highly selective gas sensors. Semiconductor metal oxide (SMO) sensors offer low cost and high stability but are limited by poor selectivity and high operating temperatures. Therefore, heterojunction engineering, morphology control, elemental doping, and surface functionalization have been widely employed to enhance their sensing performance. Among various semiconductor oxides, indium oxide (In_2O_3) has emerged as one of promising n-type sensing materials owing to its excellent electrical conductivity, high electron mobility, and strong interaction with oxidizing and reducing gases. Recent studies have demonstrated that coupling In_2O_3 with graphitic carbon nitride (g-C_3N_4) effectively suppresses electron–hole recombination and promotes interfacial charge transfer. A flexible YSZ/In_2O_3/g-C_3N_4 heterojunction sensor achieved an ultralow 50 ppb NO_2 detection limit under visible-light illumination at room temperature, demonstrating the effectiveness of heterojunction-assisted carrier separation for low-power gas sensing (Han *et al.* 2021). The sensing performance was further enhanced by incorporating plasmonic Au nanoparticles, where an Au/In_2O_3/g-C_3N_4 heterojunction exhibited a response (Rg/Ra) of 17.2 toward 1 ppm NO_2 through improved visible-light utilization and efficient photogenerated charge separation (Han *et al.* 2022).

The incorporation of conductive carbon materials has also proven effective for enhancing sensing characteristics. An In_2O_3/g-C_3N_4/rGO ternary heterostructure showed response of 2040 -100 ppm NOx, approximately seven times greater than the

corresponding binary composite, while reducing recovery and response times to 96 s, 52 s, owing to improved electron mobility and enlarged active surface area (Liu *et al.* 2023). The excellent interfacial charge-transfer capability of In_2O_3/g-C_3N_4 has also been demonstrated in photocatalytic systems. A multiporous heterojunction produced a hydrogen evolution rate of 68.7 μmol h^{-1}, representing approximately 9.3-fold improvement over pristine g-C_3N_4 due to effective suppression of electron–hole recombination (Liu *et al.* 2021). Similar improvements were reported for carbon-doped In_2O_3/g-C_3N_4 heterojunctions, which produced CO and CH_4 at rates of 152.42 and 111.31 μmol g^{-1} h^{-1}, respectively, owing to the combined effects of carbon doping, hollow tubular morphology, and type-II band alignment (Xu *et al.* 2021). These investigations clearly demonstrate that heterojunction engineering substantially enhances carrier separation, extends visible-light utilization, and provides abundant active sites, making In_2O_3/g-C_3N_4 one of promising semiconductor systems for advanced gas sensing. Elemental modification further improves catalytic activity in In_2O_3-based sensors. Hierarchical Pt-loaded/Ce-doped In_2O_3 microspheres achieved a response (Ra/Rg) of 900 -100 ppm triethylamine with detection limit of 5 ppb at 100 °C, demonstrating enhanced sensitivity and reduced operating temperature due to Pt sensitization and Ce doping (Jin *et al.* 2023).

Porous nanostructures also enhance sensing by providing abundant active sites. Hydrothermally synthesized In_2O_3 nanorods showed optimal performance toward 400 ppm CO at 350 °C, with good selectivity and stability resulting from their porous morphology (Van *et al.* 2021). Crystal-phase engineering has emerged as another effective approach. Cubic–rhombohedral In_2O_3 microspheres exhibited a response of 16.8 toward 100 ppm acetone, with rapid response and recovery times of 4.7 s and 6.0 s, due to abundant oxygen vacancies and heterophase interfaces (Cao *et al.* 2023). Transition metal oxide doping enables ppb-level detection. Cr_2O_3-doped In_2O_3 nanoflower detected isoprene below 5 ppb, showing excellent selectivity and humidity resistance against multiple interfering gases (Wu *et al.* 2021).

Core–shell structures further improve trace detection. MOF-derived In_2O_3@ZnO heterostructures enabled detection of 100 ppb acetone with a rapid 2 s response, along with improved selectivity and humidity resistance (Chen *et al.* 2023). Room-temperature sensing is attractive for low energy consumption. Porous In_2O_3–ZnO nanofibers detected toluene under 365 nm UV illumination at room temperature with excellent selectivity, demonstrating effective UV-assisted activation (Cai *et al.* 2023). Beyond gas sensing, g-C_3N_4-based materials show multifunctional capabilities. AD-CQDs/g-C_3N_4 composites reached complete degradation of 2,4-dichlorophenol within 90 min while detecting Fe^{3+} ions with a 1 nM limit (Sim et al. 2021). Additionally, CuS/g-C_3N_4 nanocomposites enabled selective detection of ibuprofen with detection of 16.01 mg L^{-1} in real samples (Borthakur *et al.* 2021). Electrochemical and photoelectrochemical sensing applications further expand their utility. A g-C_3N_4 nanotube@MoS_2 composite detected vanillin over 0.005–458.9 μM with a 4 nM limit (Nehru et al. 2023). $BiVO_4$@Bi_2O_3@g-C_3N_4 sensors detected dopamine with a 0.046 μM limit, and g-C_3N_4/Bi_2S_3 composites detected nitrite down to 0.4 nM, highlighting their environmental sensing potential (Çakar *et al.* 2022; Kogularasu *et al.* 2022).

Artificial intelligence has further improved volatile organic compound differentiation using semiconductor heterojunction sensors. CuO–ZnO sensors combined with support vector machine reached 98.13% classification accuracy, highlighting precise distinction of chemically similar gases (Kulkarni and Ghosh, 2023). Deep learning techniques have demonstrated strong capability in sensor signal analysis. A convolutional neural network predicted gamma-ray energies with an error below 0.1%, indicating efficient extraction of information from complex sensing data (Chaudhuri *et al.* 2022). Artificial neural networks have also improved environmental data processing. Recurrent neural network with neural imputation enhanced solar irradiance prediction under incomplete datasets, providing a robust monitoring framework (Girimurugan *et al.* 2023). Advanced electrochemical techniques have improved understanding of sensing interfaces. Potentiodynamic electrochemical impedance spectroscopy effectively monitored multilayer electroactive interfaces by analyzing charge-transfer and diffusion processes (Ganvir *et al.* 2024). Recent nanotechnology developments highlight nanosensors for environmental, food, and agricultural monitoring. Carbon nanomaterials, graphene derivatives, and semiconductor nanocomposites offer high sensitivity, selectivity, and rapid response (Kumari *et al.* 2025).

Despite remarkable developments in semiconductor gas sensors through heterostructure construction, structural tailoring, dopant incorporation, and noble-metal functionalization, previous investigations have predominantly emphasized sensitivity enhancement for individual gases, including NO_2, formaldehyde, triethylamine, CO, acetone, and isoprene. In contrast, comparatively few studies have addressed the selective recognition of structurally related VOCs, especially ethanol and acetone. Furthermore, the underlying sensing behaviour has mainly been described using conventional surface interaction theories, whereas detailed adsorption kinetic evaluation has rarely been considered. In particular, the application of the Langmuir-Hinshelwood kinetic framework to In_2O_3/g-C_3N_4 heterojunction gas sensors has received minimal investigation. Although ML has emerged as powerful tool for gas identification, most available reports depend on sensor arrays or electronic nose architectures instead

of an individual heterojunction sensing platform. Accordingly, this work employs hydrothermally prepared In_2O_3/g-C_3N_4 heterojunction nanoparticles for the selective recognition of ethanol and acetone by combining detailed materials characterization, Langmuir-Hinshelwood adsorption kinetic analysis, and machine learning-based classification, establishing a comprehensive and intelligent approach for highly selective VOC sensing.

2. EXPERIMENTAL METHODOLOGY

2.1 In_2O_3/g-C_3N_4 Synthesis and Characterization

The In_2O_3/g-C_3N_4 (indium oxide/graphitic carbon nitride) nanocomposite was fabricated through a simple solution-based chemical synthesis route. Reagent-grade precursors were obtained from Astron Chemicals, India, and utilized directly as received without additional treatment. Initially, graphitic carbon nitride was produced by thermally condensing melamine. A measured quantity of melamine was transferred into lidded alumina crucible and calcined in a muffle furnace at 550 °C for 4 hours using heating ramp of 5 °C min^{-1}. Following furnace cooling to ambient temperature, the resulting yellow solid was collected and pulverized into a fine g-C_3N_4 powder.

To prepare the In_2O_3/g-C_3N_4 nanocomposite, $In(NO_3)_3 \cdot xH_2O$ was initially introduced into 50 mL of distilled water and stirred until complete dissolution produced a homogeneous solution. Separately, the as-prepared g-C_3N_4 powder was suspended in distilled water and sonicated for 30 minutes to ensure effective exfoliation and uniform distribution. The dispersed g-C_3N_4 suspension was gradually incorporated into the indium precursor solution while maintaining constant agitation. Subsequently, aqueous ammonia was slowly added until the reaction medium reached pH 9–10, promoting the *in situ* deposition of indium hydroxide species over the g-C_3N_4 sheets. The suspension was further agitated for 2 h and left undisturbed for 12 hours at ambient conditions. The resulting solid was separated through centrifugation, repeatedly rinsed with deionized water and ethanol to eliminate remaining contaminants, and oven-dried on 80 °C for 12 hours. The dried intermediate was then heat-treated in air at 500 °C for 2 h, yielding a highly crystalline In_2O_3/g-C_3N_4 nanocomposite.

During wet chemical preparation of In_2O_3/g-C_3N_4, homogeneous mixing of the indium precursor and g-C_3N_4 suspension promoted uniform nucleation and controlled growth of the oxide phase on the carbon nitride surface. The alkaline medium facilitated the formation of indium hydroxide intermediates, while continuous stirring minimized particle agglomeration and ensured even distribution throughout the reaction system. Subsequent thermal treatment transformed the precursor into crystalline In_2O_3, leading to intimate interfacial contact with g-C_3N_4 and successful formation of heterojunction nanocomposite.

The phase composition and morphological characteristics of the In_2O_3/g-C_3N_4 nanocomposite were systematically examined using multiple characterization techniques, including thermogravimetric and Fourier transform infrared spectroscopy (FTIR), differential thermal analysis (TGA-DTA), powder X-ray diffraction (XRD), Raman spectroscopy, field-emission scanning electron microscopy, UV–visible spectroscopy, and N_2 adsorption-desorption measurements.

2.2 VOC Sensing

Gas-sensing evaluation was performed using a custom-built static gas testing apparatus assembled in our laboratory. The experimental setup comprised a sealed test chamber, a heating stage integrated with probe station, programmable temperature control unit, and precision source meter. The configuration of the sensing platform was comparable to the system previously established by our research group. A disc-shaped sensing pellet (10 mm diameter and 1 mm thickness) was fabricated from the calcined In_2O_3/g-C_3N_4 powder, and two parallel silver electrodes were deposited on its surface using conductive Ag paste. The fabricated pellet served as the active sensing component during all gas detection experiments.

Gas-sensing performance of the In_2O_3/g-C_3N_4 pellet was investigated at temperatures ranging from 210 to 300 °C under different concentrations of ethanol and acetone vapors. During each measurement, the electrical conductance of the sensing element was continuously monitored in ambient air (C_a) and after exposure to the analyte atmosphere (C_g) through the silver strip electrodes. For the n-type semiconducting sensing material, the response (S) was determined from the ratio C_g/C_a. The quantity (V) of liquid VOC (99.99% purity) required to produce the desired gas concentration (ppm) inside the sensing chamber was calculated using the following expression (Eq. 1) (Chaudhary and Nehra, 2021).

$$V = \frac{Cv_aM}{2.46\times10^7\times D} \quad \ldots (1)$$

In this equation, C specifies the required vapor concentration, V_a indicates internal volume of the sensing chamber (mL), M corresponds to the molecular mass of ethanol or acetone (g mol^{-1}), and D refers to the density of the respective liquid analyte (g mL^{-1}).

2.3 Machine Learning Methodology

The machine learning dataset was generated from the experimental gas-sensing results obtained using

the In_2O_3/g-C_3N_4 sensor, comprising 120 experimental observations recorded at analyte concentrations of 250–1000 ppm and operating temperatures of 210–300 °C. The classification task aimed to identify the target vapor, namely ethanol or acetone, using gas concentration, operating temperature, sensor response (Cg/Ca), recovery time, and response time as input features. To accomplish this objective, Support Vector Machine (SVM), Extreme Gradient Boosting (XGBoost), Artificial Neural Network (ANN), Random Forest (RF), and Light Gradient Boosting Machine (LightGBM) algorithms were developed for data preparation, model development, and comparative assessment of classification performance (Selamneni *et al.* 2021). Since the sensing measurements were directly acquired from the In_2O_3/g-C_3N_4 experiments, the raw dataset was examined for redundant entries and incomplete records before model construction. Following preprocessing, repeated observations and non-informative samples were discarded, resulting in a refined dataset containing 120 independent sensing instances. This processed dataset was subsequently divided into 5% training and 25% testing subsets, and predictive capability were assessed by accuracy, recall, precision, ROC–AUC and F1-score metrics. To ensure reliable model generalization and reduce the possibility of overfitting, a hold-out validation strategy with data normalization prior to model training was adopted for performance assessment and comparison of the classifiers in distinguishing ethanol from acetone vapors. The complete machine learning workflow developed from the experimental sensing measurements is illustrated in Fig. 1.

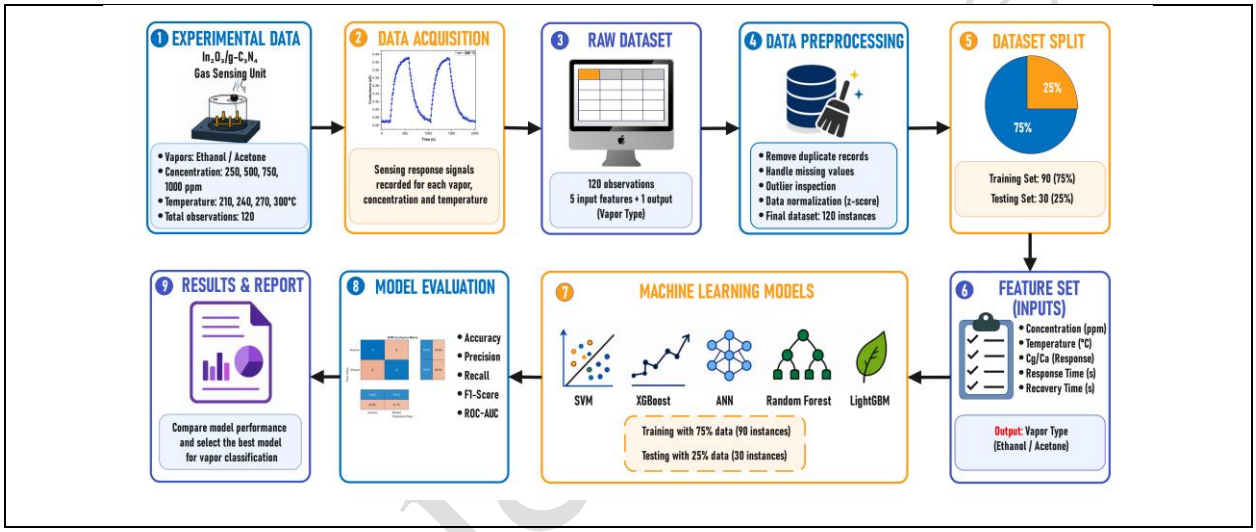

Fig. 1: ML workflow for vapor classification

3. RESULTS AND DISCUSSION

3.1 Structural and Microstructural Analysis

The thermal behaviour of as-prepared In_2O_3/g-C_3N_4 precursor was investigated by thermogravimetric and differential thermal analysis (TGA-DTA) from room temperature to 1000°C. The corresponding TGA-DTA are presented in Fig. 2. Two major mass-loss regions were observed during heating. The initial reduction below 150 °C resulted from removal of physically adsorbed moisture and residual volatile species, whereas the subsequent decrease between 150 and 420 °C were attributed to decomposition of precursor compounds and progressive formation of the In_2O_3/g-C_3N_4 heterostructure. Beyond approximately 450 °C, the TGA curve became nearly constant with a residual weight of about 71.5–72 wt.%, confirming the completion of thermal conversion and the formation of a thermally stable crystalline product. The DTA curve exhibited a small endothermic peak near 100 °C, followed by a pronounced exothermic peak centered at approximately 250–260 °C, corresponding to the decomposition and crystallization processes associated with nanocomposite formation. A weak broad exothermic feature around 380–420 °C further indicates the completion of crystallization before the thermal profile stabilized at higher temperatures.

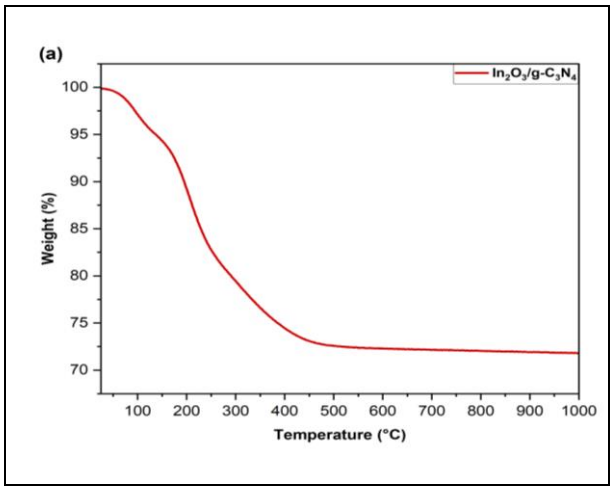

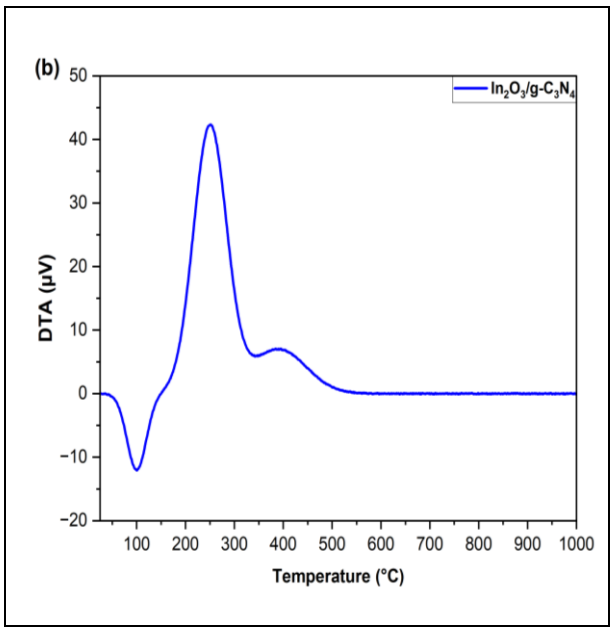

Fig. 2: Thermal decomposition by (a) TGA and (b)DTA

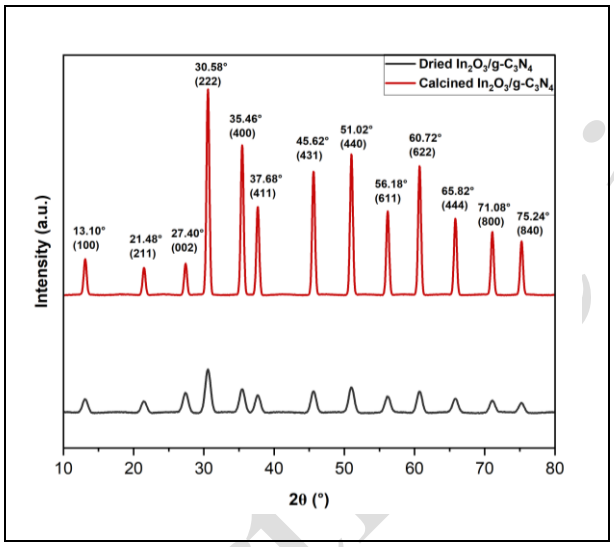

Fig. 3: XRD phase identification analysis

Fig. 3 displays XRD of In_2O_3/g-C_3N_4 samples recorded before and after calcination. The diffraction profile confirms the successful formation of a highly crystalline heterojunction nanocomposite. The characteristic reflections of cubic In_2O_3 are clearly observed together with typical diffraction peaks of g-C_3N_4, demonstrating the coexistence of both constituent phases without the appearance of detectable impurity peaks. Following calcination, diffraction maxima become more intense and sharper, showing improved crystallinity and improved structural ordering of In_2O_3/g-C_3N_4 nanocomposite.

The XRD data of In_2O_3/g-C_3N_4 nanocomposite were utilized to determine the crystal phase, lattice constants, and average crystallite dimension. The crystallite size was estimated from the diffraction profile using Scherrer equation, where full width at half maximum of the dominant (222) reflection located at 2θ = 30.58° was employed for the calculation (Liu *et al.* 2022);

$$D = \frac{0.9\lambda}{\beta \cos\theta} \quad \ldots (2)$$

In the Scherrer equation, D denotes the mean crystallite dimension, λ is the wavelength of incident X-ray radiation, β corresponds to full width at half maximum of selected diffraction peak, and θ represents associated Bragg diffraction angle. Average crystallite sizes calculated for dried and calcined In_2O_3/g-C_3N_4 samples were approximately 14.8 nm and 18.3 nm, respectively. A comparison of the diffraction profiles showed progressively sharper and narrower reflections after calcination, indicating enhanced crystallinity and growth of crystallites as the heat-treatment temperature increased.

Fig. 4(a) compares FTIR spectra of dried In_2O_3/g-C_3N_4 precursor and the sample calcined at 600 °C. The spectra confirm the successful formation of the heterojunction through the characteristic peaks of both constituent phases. The stretching modes associated with C–N and C=N of g-C_3N_4 framework are clearly observed, while the breathing vibration of the triazine/heptazine ring further verifies graphitic carbon nitride structure. In the lower wavenumber region, the peak assigned to the In–O lattice vibration confirms the formation of crystalline In_2O_3. Following calcination, the characteristic peaks become more distinct with slight peak shifts, indicating improved crystallinity and stronger interfacial interaction between In_2O_3 and g-C_3N_4 without altering the fundamental chemical structure (Wankhade and Pedhekar, 2025).

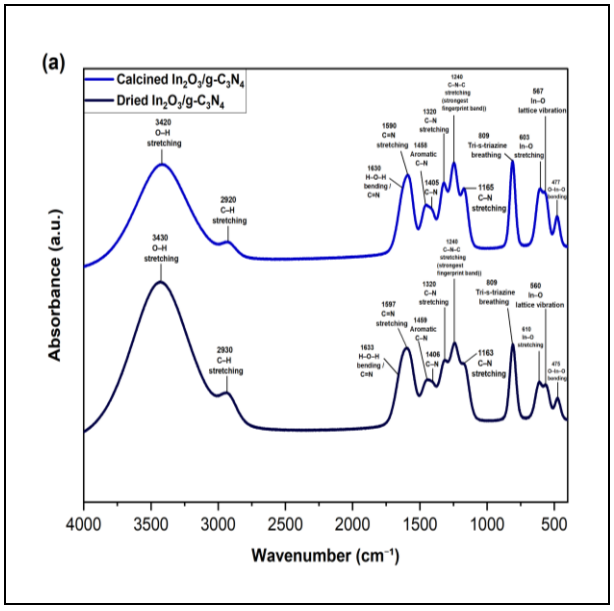

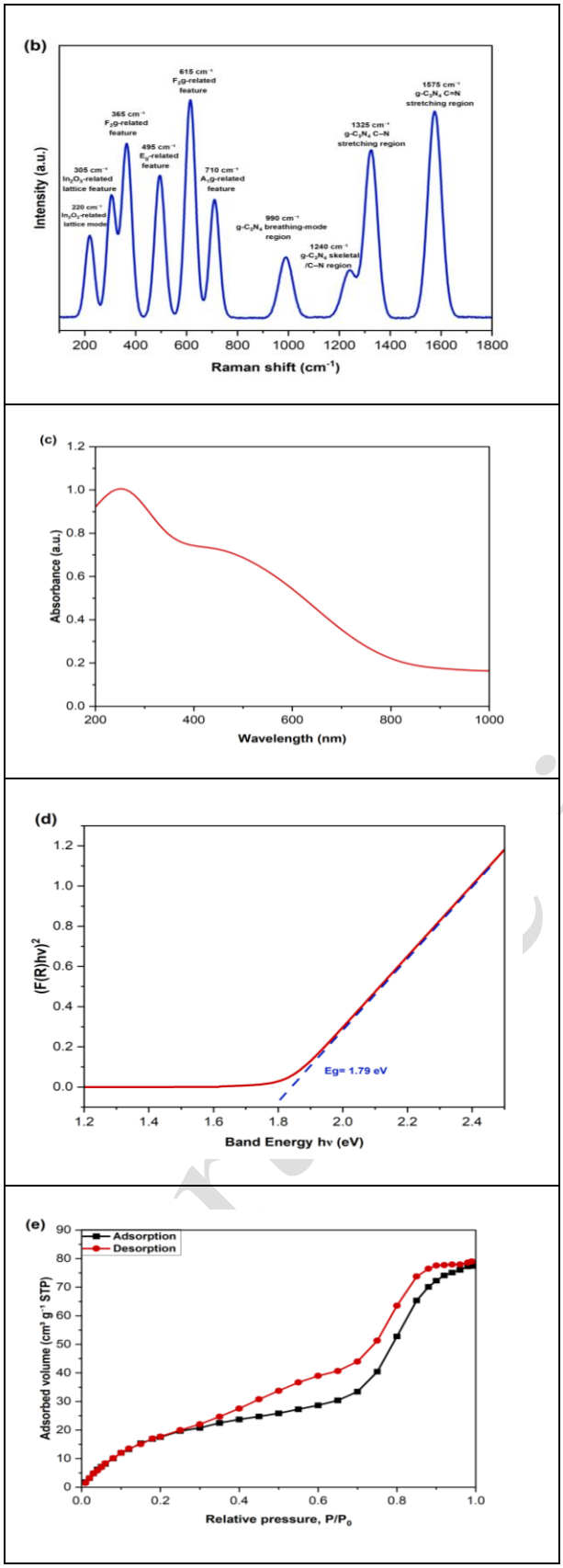

Fig. 4: (a) FTIR spectral characterization (b) Raman spectral analysis (c) Optical absorption spectra (d) Optical band-gap energy and (e) BET adsorption–desorption analysis

The In_2O_3/g-C_3N_4 nanocomposite consists of cubic In_2O_3 integrated with layered g-C_3N_4, forming a well-defined heterojunction structure. The Raman spectrum shown in Fig. 4(b) exhibits characteristic vibrational modes of components, confirming successful incorporation of In_2O_3 onto the g-C_3N_4 framework. The observed Raman bands originate from lattice vibrations of crystalline In_2O_3, whereas the carbon nitride phase displays its typical graphitic skeletal breathing mode, verifying the coexistence of the two phases. Fig. 4(c) presents the UV–visible reflectance spectrum of the calcined In_2O_3/g-C_3N_4 nanocomposite recorded between 200 and 1000 nm. The optical band-gap energy was determined from the diffuse reflectance data using Kubelka-Munk approach, where absorption coefficient (α) was considered proportional to Munk function (F(R)), under assumption of a constant scattering coefficient, as expressed by the following equation (Jasim and Sameer, 2024).

$$F(R) = \alpha = \frac{(1-R)^2}{2R} \quad \ldots (3)$$

where R denotes obtained reflectance.

Direct optical band-gap energy of In_2O_3/g-C_3N_4 nanocomposite was determined using the Tauc relation:

$$F(R)h\vartheta = A\left(h\vartheta - E_g\right)^{1/2} \quad \ldots (4)$$

Using Equation. 3, Eqn. 4 is written as

$$(\alpha h\vartheta)^2 = A\left(h\vartheta - E_g\right) \quad \ldots (5)$$

Based on Eq. (5), the optical band-gap energy was analysed from Tauc plot presented in inset of Fig. 4(d). The calculated optical band-gap energy of the In_2O_3/g-C_3N_4 nanocomposite was 1.94 eV. The N_2 adsorption-desorption together with the Barrett-Joyner-Halenda pore-size distribution of calcined sample is displayed in Fig. 4(e). The adsorption profile exhibits type IV isotherm accompanied by hysteresis loop in the higher relative pressure region, confirming the existence of a mesoporous structure.

The prepared In_2O_3/g-C_3N_4 powder was compressed into disc-shaped pellets for gas-sensing measurements. The FESEM image presented in Fig. 5(a) reveals a densely packed microstructure composed of irregularly shaped agglomerated particles with good interparticle connectivity, providing continuous pathways for charge transport during gas sensing. The surface exhibits numerous interconnected voids and porous regions distributed throughout the agglomerated structure, which are expected to facilitate gas diffusion and provide abundant active sites for surface adsorption, thereby enhancing the sensing performance of the In_2O_3/g-C_3N_4 chemiresistor. The elements determined from EDX analysis (Fig. 5(b)) confirm the successful

incorporation of In, C, O, and N, confirming the formation of In_2O_3/g-C_3N_4 heterojunction nanocomposite.

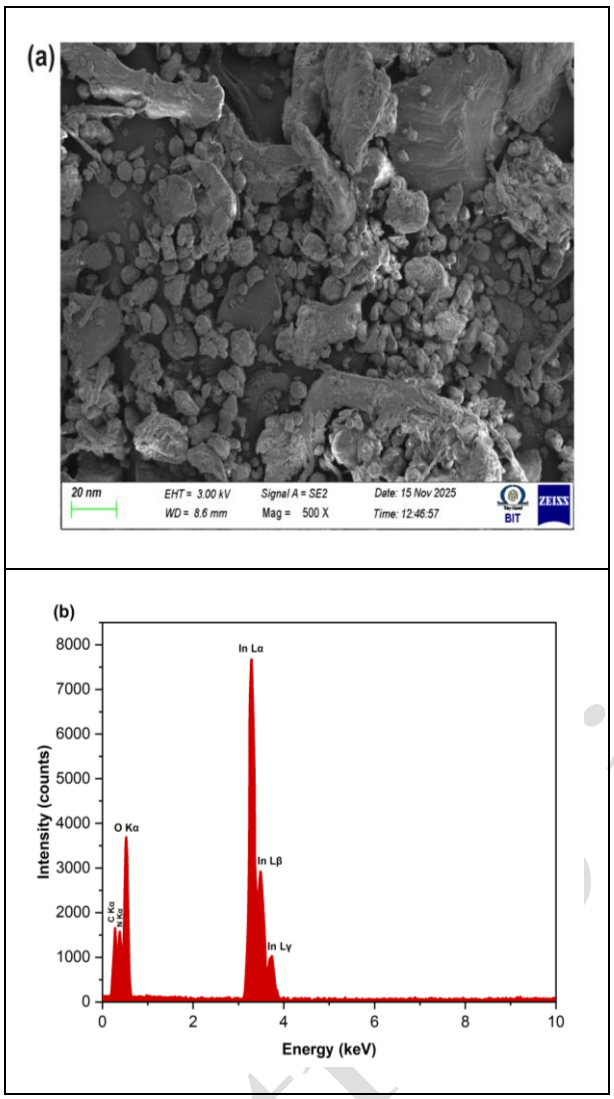

Fig. 5: (a) FESEM morphology of In_2O_3/g-C_3N_4 and (b) EDX elemental composition analysis

3.2 VOC Sensing Performance Analysis

The variation in electrical conductivity originates from the successive interaction between chemisorbed oxygen species and reducing analytes, namely ethanol and acetone. As illustrated, heating the sensing element promotes adsorption of atmospheric oxygen onto In_2O_3/g-C_3N_4 surface in the form of ionic oxygen species (O_{ad}^-) (Eq. 6). These adsorbed species capture conduction-band electrons, producing an electron-depletion region that lowers electrical conductivity of sensing layer. Upon exposure to reducing vapors, adsorbed oxygen ions react with the gas molecules to generate oxidized products (RO_{ad}) (Eq. 7), simultaneously releasing trapped electrons back into sensing material and thereby increasing its conductivity. During the regeneration stage, the reaction products desorb as gaseous species (RO_g), while fresh oxygen is chemisorbed from the surrounding atmosphere (Eq. 8), restoring the initial electron-depletion layer and decreasing conductivity. Furthermore, pelletization of In_2O_3/g-C_3N_4 powder produces interconnected macroporous and mesoporous networks that provide abundant adsorption sites and efficient diffusion pathways for gaseous molecules, as discussed in the subsequent kinetic analysis. Consequently, morphological optimization plays significant role in improving gas-sensing by enlarging accessible surface area and promoting rapid mass transport (Yang *et al.* 2021).

$$O_2 + e^- \leftrightarrow O^-/O^{2-}/O_{2ad}^- \quad \ldots (6)$$

$$R_g + O_{ad}^- \xrightarrow{k_a} RO_{ad} \quad \ldots (7)$$

$$RO_{ad} \xrightarrow{k_d} RO_g \uparrow \quad \ldots (8)$$

Fig. 6(a) and (b) show dynamic conductance profiles of In_2O_3/g-C_3N_4 sensor during exposure to acetone and ethanol over the operating temperature interval of 210–300 °C. Two successive sensing cycles were performed to determine the optimum working temperature for detecting both volatile organic compounds. As illustrated in Fig. 6(c), the sensing response of In_2O_3/g-C_3N_4 device progressively increases with increasing operating temperature, confirming the characteristic behaviour of an n-type semiconducting sensor. Comparable temperature-dependent response enhancement has been widely documented and is generally attributed to accelerated chemisorption of oxygen species and resulting increase in surface reaction kinetics

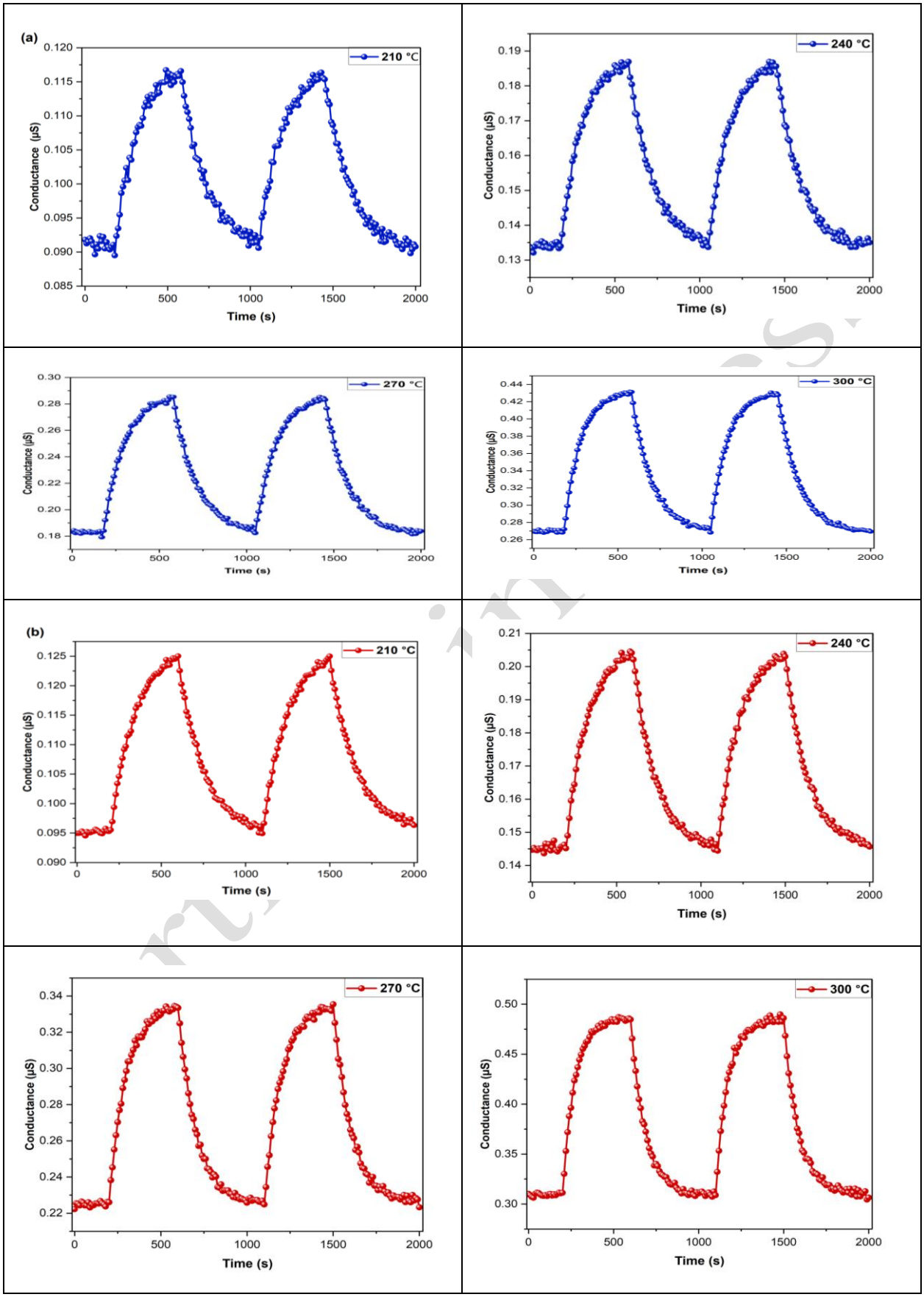
(a)
210 °C
240 °C
270 °C
300 °C
(b)
210 °C
240 °C
270 °C
300 °C
Conductance (µS)
Time (s)

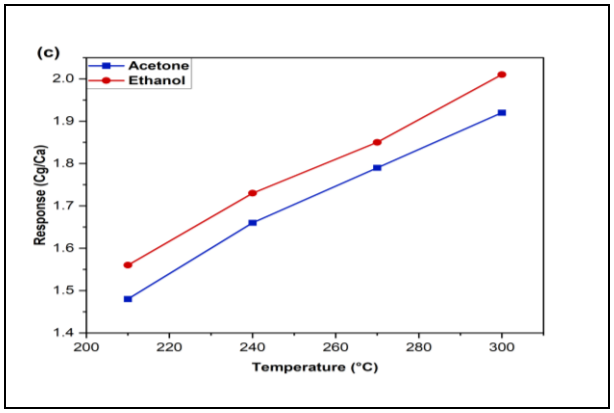

Fig. 6: (a) Acetone conductance transients at temperatures, (b) Ethanol conductance transients at temperatures and (c) Vapor sensing response comparison

Fig. 7(a) and 7(b) illustrate the conductance response of the In_2O_3/g-C_3N_4 sensor upon exposure to ethanol and acetone vapors over a concentration range of 250–1000 ppm. The sensing signal exhibits an approximately proportional increase at lower analyte concentrations, whereas a gradual deviation from linearity becomes evident at higher concentrations, as presented in Fig. 7(c). The repeatability of sensor was further examined at 750 ppm ethanol and an operating temperature of 300 °C by performing eight continuous sensing–recovery cycles (Fig. 7(d)) demonstrating stable and reproducible performance. Previous investigations have also shown that noble-metal modification can markedly improve gas-sensing characteristics. For example, Au-decorated In_2O_3 nanoparticles showed response value of 106 toward 100 ppm ethanol while reducing the optimum operating from 240 °C to 200 °C, highlighting the catalytic contribution of Au to ethanol detection(Fang *et al.* 2022). The excellent operational stability demonstrated by the In_2O_3/g-C_3N_4 sensor highlights its suitability for practical gas-monitoring applications. Moreover, its rapid response and recovery behaviour, satisfactory selectivity, and consistent reproducibility indicate that the developed sensing platform is a reliable candidate for efficient ethanol detection.

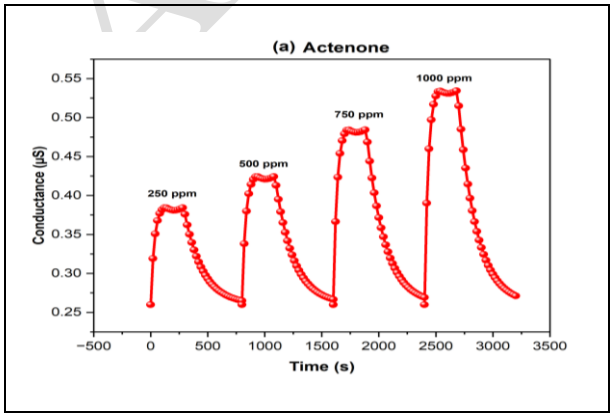

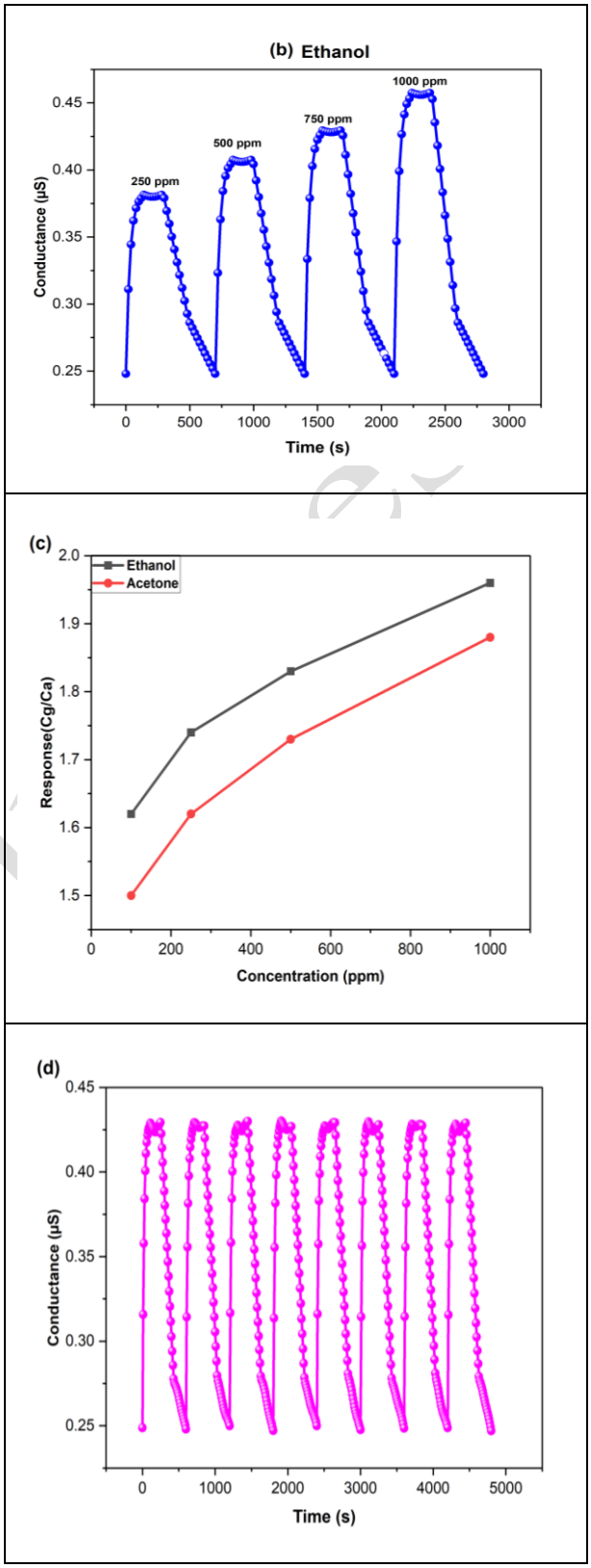

Fig. 7: (a) Acetone conductance transient responses, (b) Ethanol conductance transient responses, (c) Concentration-dependent sensing response and (d) Ethanol response−recovery cycling

3.3 Response Transient Kinetic Analysis

Kinetic modelling was employed to establish the relationship between the experimental sensing behaviour and the proposed surface reaction pathway, thereby providing insight into interaction of analyte molecules with In_2O_3/g-C_3N_4 sensing layer. As described previously, exposure of the sensor to ethanol or acetone results in the oxidation of the target molecules by the chemisorbed oxygen species (Eq. 7), producing RO_{ad} intermediates on the surface. Under the assumption of monolayer adsorption at a fixed operating temperature (T), measured conductance transients were interpreted by Langmuir-Hinshelwood adsorption kinetic model. Considering that the reaction represented by Eq. 7 governs the overall process, the formation rate of RO_{ad} may be expressed as follows (Samuel *et al.* 2024):

$$\frac{d[RO_{ad}]}{dt} = k_a[R_g][O_{ad}^-] - k_d[RO_{ad}] \quad \ldots (9)$$

Assuming that, at a given time (t), a fractional surface coverage of θ is occupied by the oxidized reaction intermediates (RO_{ad}) formed on In_2O_3/g-C_3N surface, remaining fraction (1−θ) is considered to be covered by chemisorbed oxygen species (O_{ad}^-). If the concentration of the introduced reducing analyte (ethanol or acetone) is represented by Cg, the rate expression derived from Eq. (9) can be written as follows:

$$\frac{d\theta}{dt} = k_a(1-\theta)Cg - K_d\theta \quad \ldots (10)$$

k_a and k_d shows adsorption and desorption constants.

$$k_a = \frac{SNoKo}{(2\pi MRT)^{1/2}} \exp\left(-\frac{E_a}{RT}\right) \quad \ldots (11)$$

The Equation. (10) with boundary condition, at $t = 0, \theta = 0$ (Shanavash *et al.* 2026),

$$\theta(t) = \left[\frac{k_aC_g}{k_aC_g+k_d}\right]\{1 - \exp[-(k_aC_g + k_d)t]\} \quad \ldots (12)$$

Equation (12) was simplified as,

$$\theta(t) = \left[\frac{k_1-k_d}{k_1}\right]\{1 - \exp[-k_1t]\} \quad \ldots (13)$$

where,

$$k_1 = k_aC_g + k_d \quad \ldots (14)$$

when $t \to \infty, \theta = \theta_0$, Eqn. (13) can be written as,

$$\theta(t) = \theta_0\{1 - \exp[-k_1t]\} \quad \ldots (15)$$

When

$$k_1 \sim \frac{1}{\tau_{res}} \quad \ldots (16)$$

$$\theta(t) = \theta_0\left\{1 - \exp\left[-\frac{t}{\tau_{res}}\right]\right\} \quad \ldots (17)$$

$$G_t = G_o + G_1\left\{1 - \exp\left[-\frac{t}{\tau_{1(res)}}\right]\right\} \quad \ldots (18)$$

The conductance response profiles of the In_2O_3/g-C_3N_4 chemiresistive sensor recorded during ethanol and acetone detection at operating temperatures of 210, 240, 270, and 300 °C were initially analysed using Eq. (18). Nevertheless, this model produced unsatisfactory agreement with the experimental data, yielding regression coefficients of $R^2 < 0.80$. Improved fitting was achieved by considering adsorption over two independent surface sites and applying Eq. (19), resulting in excellent agreement with $R^2 > 0.98$ for both target vapors at all investigated temperatures, as presented in Fig. 8(a) and (b). Corresponding fitting parameters for acetone and ethanol are summarized in Tables 1 and 2. In addition, baseline conductance increased progressively with operating temperature for analytes, whereas primary response time constant exhibited a decreasing trend.

Table 1. Conductance transient fitting parameters for ethanol

Temperature (°C)	$\tau_1(s)$	τ_2(s)	$G_0(S^{-1})$	$G_1(S^{-1})$	$G_2(S^{-1})$
210	42.0	10.5	0.083	0.073	0.028
240	9.8	2.7	0.142	0.034	0.011
270	17.5	4.8	0.200	0.145	0.047
300	22.0	5.5	0.290	0.115	0.040

Table 2. Conductance transient fitting parameters for acetone

Temperature (°C)	$\tau_1(s)$	τ_2(s)	$G_0(S^{-1})$	$G_1(S^{-1})$	$G_2(S^{-1})$

210	34.5	8.2	0.062	0.037	0.014
240	22.8	5.6	0.063	0.038	0.012
270	41.5	7.4	0.300	0.055	0.022
300	48.0	6.8	0.275	0.105	0.047

$$(t) = G_o + G_1\left\{1 - \exp\left[-\frac{t}{\tau_{1(res}}\right]\right\} G + G_2\left\{1 - \exp\left[-\frac{t}{\tau_{2(res)}}\right]\right\} \quad \ldots (19)$$

In this model, G_0 represents the initial electrical conductance of the In_2O_3/g-C_3N_4 sensing layer, whereas τ_1 and τ_2 denote the first and second response time constants corresponding to two distinct adsorption regions. These regions arise from the hierarchical pore architecture of the sensing pellet, comprising both macroporous and mesoporous domains. The pellet is formed from partially fused secondary agglomerates (grains), each consisting of numerous nanoscale primary crystallites. Consequently, larger pores are generated between neighbouring grains, while smaller nanopores exist among the primary crystallites. Owing to the different gas-transport mechanisms operating within these pore networks (molecular diffusion through macropores and Knudsen diffusion within mesopores), the overall adsorption and reaction kinetics proceed at different rates.

Now assuming $k_d \ll k_a C_g$, Eqn. (14) can be rewritten as,

$$k_1 = k_a C_g \quad \ldots (20)$$

From Equation (11), deduce

$$k_a = A\exp\left(-\frac{Ea}{k_B T}\right) \quad \ldots (21)$$

A were pre-exponential constant and k_B were Boltzmann constant

From Equation 16, 20 and 21, it is rewritten as

$$\tau . C_g = A^{-1}\exp\left(\frac{Ea}{k_B T}\right) \quad \ldots (22)$$

$$\ln(\tau) = \text{const} + \frac{Ea}{k_B T} \quad \ldots (23)$$

The relationship between ln(τ_1) and 1/T for the In_2O_3/g-C_3N_4 sensor is shown in Fig. 8(c). The activation energy (E_a) was obtained from the slope of the linear regression according to Eq. (23). For 1000 ppm analyte concentration, the calculated chemisorption activation energies were 0.37 eV for acetone and 0.28 eV for ethanol. The lower E_a associated with ethanol indicates a more favorable surface reaction on In_2O_3/g-C_3N_4 sensing layer, thereby producing a comparatively higher sensing response. Since τ_2 represents adsorption within the macroporous network, where intermolecular interactions become significant, reliable estimation of activation energy is difficult. Conversely, τ_1 is associated with the mesoporous region, where gas transport is governed predominantly by pore diffusion and gas–surface interactions. Therefore, the activation energy analysis was performed using only the τ_1 values.

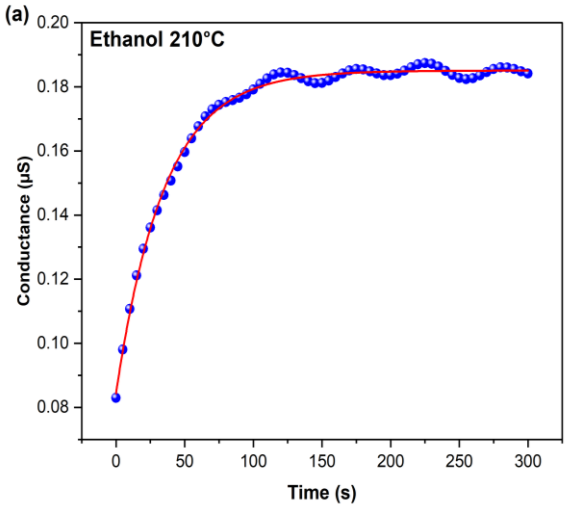

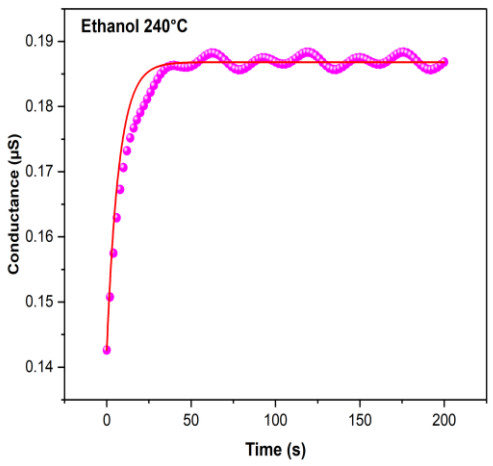

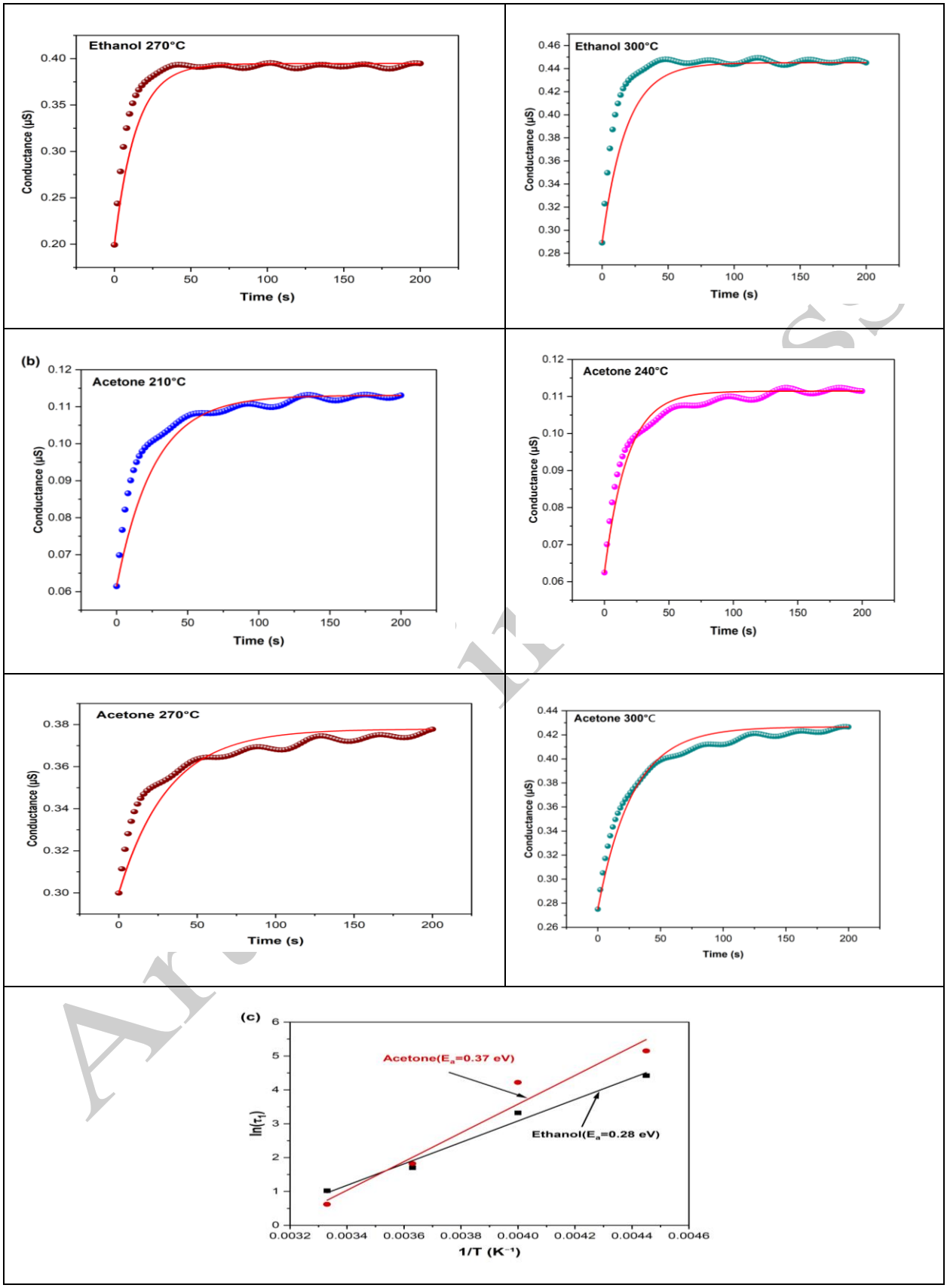

Fig. 8: Conductance transients and activation energy analysis

3.4 LDA-based Vapor Discrimination

Linear Discriminant Analysis is a supervised statistical technique that projects multidimensional data onto a lower-dimensional space while maximizing class separability. In contrast to Principal Component Analysis, which identifies maximum variance without considering class information, LDA incorporates predefined class labels to determine discriminant directions that provide the greatest distinction among categories. In this study, LDA was applied to the sensing responses of the In_2O_3/g-C_3N_4 chemiresistive sensor obtained for ethanol and acetone at concentrations between 250 and 1000 ppm over an operating temperature range of 210–300 °C. As illustrated in Fig. 9, the two analytes form clearly separated clusters with negligible overlap, demonstrating the excellent discrimination capability of the In_2O_3/g-C_3N_4 sensor toward ethanol and acetone.

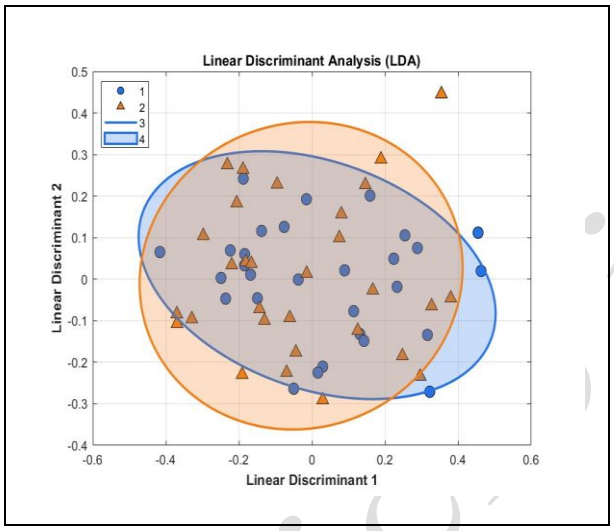

Fig. 9: Linear discriminant analysis of vapors

3.5 ML Model Evaluation

The predictive performance of the classification models exhibited clear variations when evaluated using the processed sensing dataset acquired from the In_2O_3/g-C_3N_4 sensor. Support Vector Machine produced an overall accuracy of 77.08%, together with precision of 77.13%, recall of 77.08%, F1-score of 77.07%, and ROC-AUC of 0.7717. In comparison, Random Forest delivered superior classification capability, achieving 93.33% accuracy, 93.33% recall, 93.33% precision, F1-score of 93.33%, and a ROC-AUC of 0.9956. XGBoost achieved 90.00% accuracy, 91.67% precision, 90.00% recall, F1-score of 89.90%, and ROC-AUC of 0.9600. LightGBM achieved 93.33% precision, 93.33% accuracy, 93.33% recall, F1-score of 93.33%, and ROC-AUC of 0.9822. Artificial Neural Network showed highest predictive efficiency, achieving 100% accuracy, precision, recall, F1-score, and ROC-AUC (Henriquez *et al.* 2023).

Unlike the other classifiers, ANN demonstrated complete predictive success on the processed dataset obtained from the In_2O_3/g-C_3N_4 sensor, achieving 100% accuracy, precision, recall, F1-score, and ROC-AUC. Random Forest also exhibited excellent predictive performance, recording 93.33% accuracy, 93.33% precision, 93.33% recall, F1-score of 93.33%, and ROC-AUC value of 0.9956. LightGBM achieved 93.33% precision, 93.33% accuracy, 93.33% recall, F1-score of 93.33%, and ROC-AUC of 0.9822. XGBoost attained 90.00% accuracy, 91.67% precision, 90.00% recall, F1-score of 89.90%, and ROC-AUC of 0.9600, whereas SVM produced 77.08% accuracy, 77.13% precision, 77.08% recall, F1-score of 77.07%, and ROC-AUC of 0.7717. A detailed summary of the predictive performance of all investigated classification algorithms is provided in Table 3

Table 3. Classification performance of machine learning models

Model	Accuracy	Precision	Recall	F1 Score	ROC AUC
Support Vector Machine	0.7708	0.7713	0.7708	0.7707	0.7717
Extreme Gradient Boosting	0.9000	0.9167	0.9000	0.8990	0.9600
Artificial Neural Network	1.0000	1.0000	1.0000	1.0000	1.0000
Light Gradient Boosting Machine	0.9333	0.9333	0.9333	0.9333	0.9822
Random Forest	0.9333	0.9333	0.9333	0.9333	0.9956

A detailed interpretation of the classification outcomes obtained from the In_2O_3/g-C_3N_4 sensing dataset can be achieved through the corresponding confusion matrices, which summarize numbers of true positives, true negatives, false positives, and false negatives of each classifier. Support Vector Machine exhibited moderate classification performance with a number of misclassifications, resulting in an overall accuracy of

77.08%. Random Forest improved the classification capability by reducing the number of incorrectly classified samples and achieved an accuracy of 93.33%. LightGBM classifier also demonstrated reliable prediction performance with an accuracy of 93.33%, indicating balanced classification between ethanol and acetone vapors. Among the ensemble learning methods, XGBoost achieved an accuracy of 90.00%, correctly identifying the majority of vapor samples with only a few misclassifications. The ANN classifier demonstrated complete discrimination between ethanol and acetone vapors by correctly classifying all testing samples without any classification errors.

Overall, the confusion matrices presented in Fig. 10 demonstrate that the SVM, RF, XGBoost, LightGBM, and ANN models successfully distinguished ethanol and acetone vapors with varying classification performance. Among the investigated classifiers, ANN achieved error-free prediction, while RF and LightGBM also exhibited excellent predictive capability by minimizing classification errors. XGBoost demonstrated reliable classification performance with only a few misclassifications, whereas SVM produced comparatively more misclassifications but still provided satisfactory performance for vapor classification using gas concentration, operating temperature, sensor response (Cg/Ca), response time, and recovery time as input features.

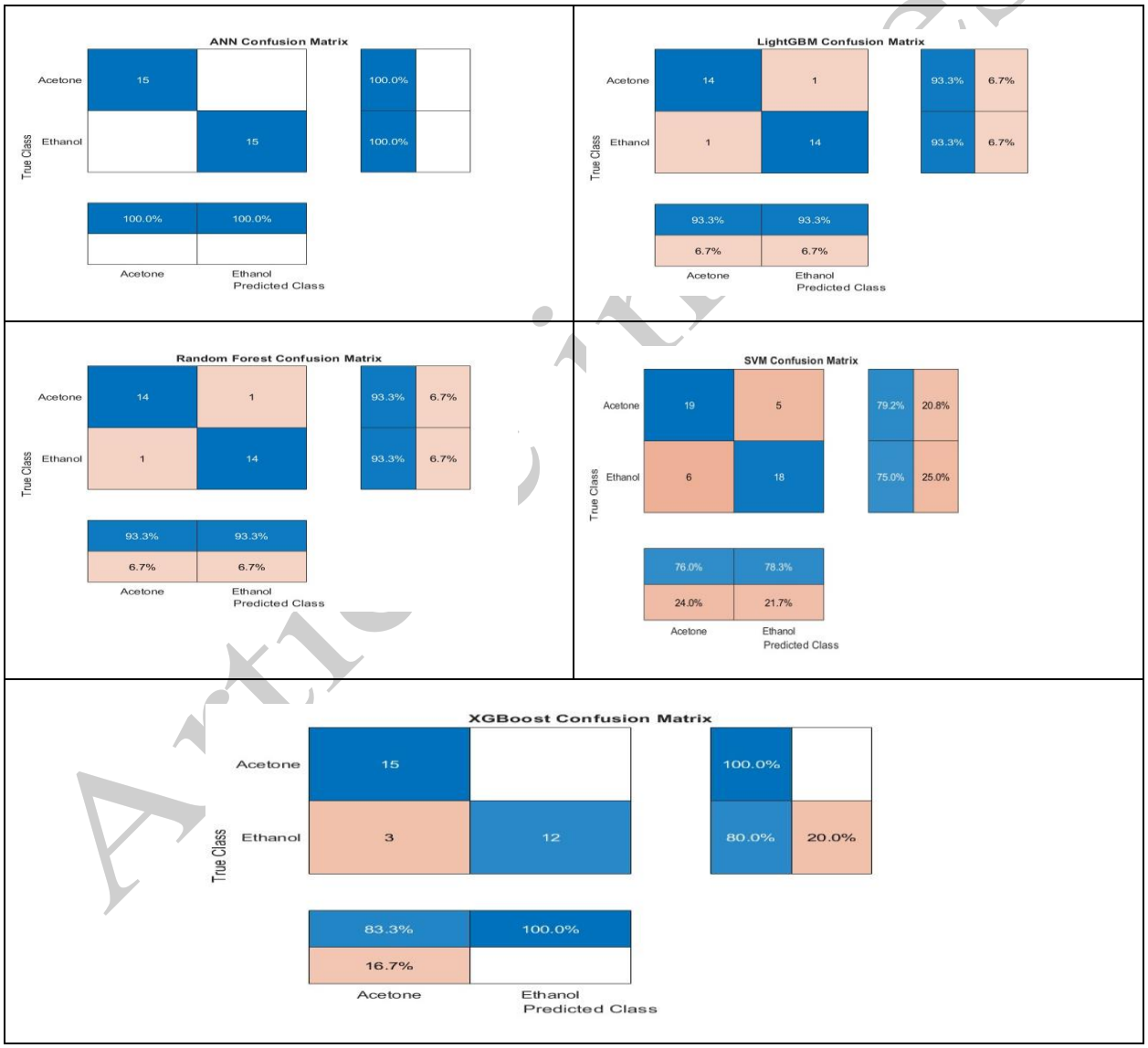

Fig. 10: Confusion matrices of machine learning classification models

Fig. 11 shows the Receiver Operating Characteristic (ROC) curves together with the corresponding Area Under the Curve (AUC) values for the classification models developed using the sensing dataset obtained from the In_2O_3/g-C_3N_4 sensor. The ROC plots illustrate the ability of all algorithms to distinguish

ethanol and acetone over a wide range of decision thresholds by representing the balance between the true-positive and false-positive rates. Models with larger AUC values exhibit superior discrimination capability and, consequently, greater predictive reliability. As a widely accepted evaluation metric, the AUC quantifies the effectiveness of a classifier in distinguishing positive and negative categories. Its value ranges from 0 to 1, where 1.0 indicates perfect classification performance, whereas values of 0.5 or lower represent prediction accuracy comparable to random guessing. Among the investigated classifiers, the ANN model achieved an AUC value of 1.0000, indicating perfect discrimination capability. Random Forest also demonstrated excellent performance with an AUC of 0.9956, followed by LightGBM with an AUC of 0.9822, XGBoost with an AUC of 0.9600, and SVM with an AUC of 0.7717. These results confirm the effectiveness of the developed machine learning models for distinguishing ethanol and acetone vapors using gas concentration, operating temperature, sensor response (Cg/Ca), response time, and recovery time as input features.

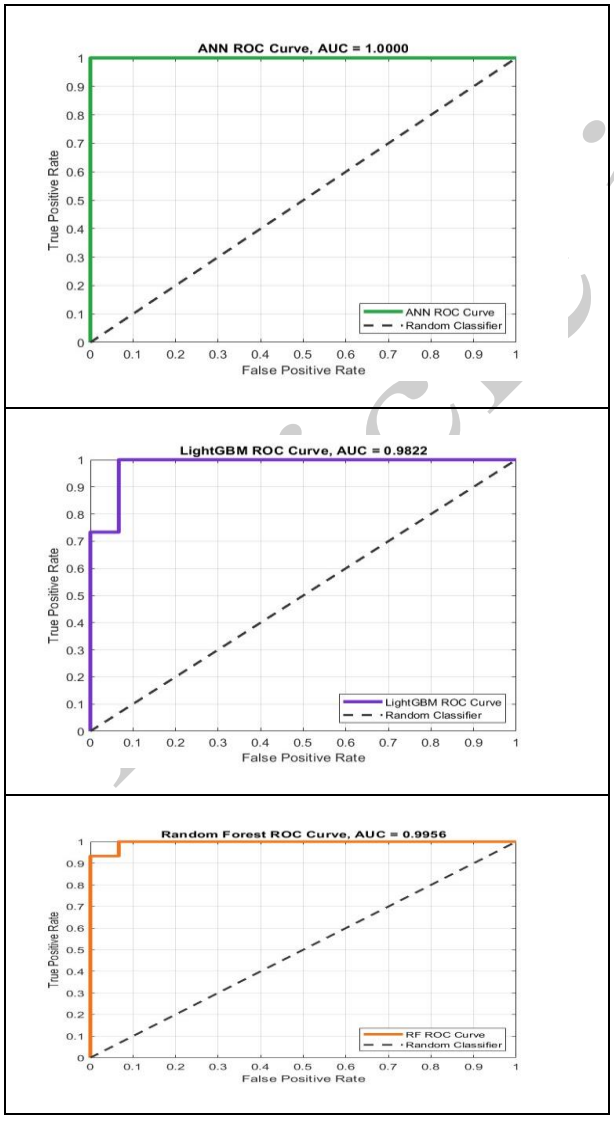

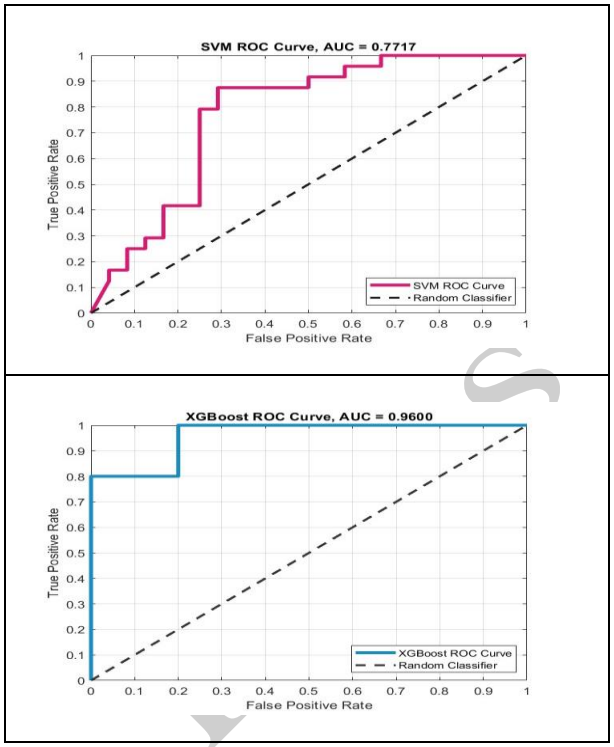

Fig. 11: ROC analysis of ML models

For the sensing dataset generated from the In_2O_3/g-C_3N_4 sensor, SVM, LightGBM, RF, XGBoost and ANN classifiers achieved AUC values of 0.7717, 0.9822, 0.9956, 0.9600, and 1.0000, respectively. The SVM exhibited comparatively lower discrimination capability than the remaining classifiers, whereas LightGBM, RF, and XGBoost demonstrated excellent predictive performance with high AUC values. Among all the investigated models, ANN attained an AUC of 1.0000, indicating outstanding classification performance. These findings confirm that the developed machine learning models are highly suitable for identifying vapor species from the In_2O_3/g-C_3N_4 sensing data using gas concentration, operating temperature, sensor response (Cg/Ca), response time, and recovery time as input variables.

4. CONCLUSIONS

This investigation establishes a comprehensive strategy by combining the sensing characteristics of In_2O_3/g-C_3N_4 with adsorption kinetic analysis and machine learning techniques to improve the differentiation of ethanol and acetone based on conductance response transients. Structural characterization and gas-sensing evaluation confirmed the effectiveness of the developed sensing material. The comparatively stronger ethanol response was successfully interpreted through the Langmuir–Hinshelwood kinetic model. Furthermore, the experimental sensing dataset was analysed using SVM, XGBoost, ANN, RF, and LightGBM algorithms to

distinguish the response patterns of ethanol and acetone. Among all evaluated classifiers, the ANN model achieved the highest classification performance, followed by Random Forest, LightGBM, XGBoost, and SVM, demonstrating the effectiveness of machine learning techniques for selective vapor classification. Consequently, the proposed methodology provides a robust framework for the selective identification of chemically similar volatile organic compounds through the combined application of In_2O_3/g-C_3N_4 sensing materials and machine learning approaches.

FUNDING

This research received no specific grant from any funding agency in the public, commercial, or not-for-profit sectors.

CONFLICTS OF INTEREST

The authors declare that there is no conflict of interest.

COPYRIGHT

REFERENCES

Borthakur, P., Boruah, P. K. and Das, M. R., Facile synthesis of CuS nanoparticles on two-dimensional nanosheets as efficient artificial nanozyme for detection of Ibuprofen in water, *J. Environ. Chem. Eng.,* 9(1), 104635 (2021). https://doi.org/10.1016/j.jece.2020.104635

Cai, Z., Park, J. and Park, S., Porous In_2O_3–ZnO nanofiber-based sensor for ultrasensitive room-temperature detection of toluene gas under UV illumination, *J. Mater. Res. Technol*., 24, 2482–2499 (2023). https://doi.org/10.1016/j.jmrt.2023.03.162

Çakar, S., Çakiroğlu, B., Şen, Ş. and Özacar, M., A photo-sensitive $BiVO_4$@Bi_2O_3@g-C_3N_4 sensor for the detection of dopamine, *Microchem. J.,* 178, 107360 (2022). https://doi.org/10.1016/j.microc.2022.107360

Cao, E., Wu, L., Zhang, Y., Sun, L., Yu, Z. and Nie, Z., Hydrothermal synthesis of cubic-rhombohedral-In_2O_3 microspheres with superior acetone sensing performance, *Appl. Surf. Sci.,* 613, 156045 (2023). https://doi.org/10.1016/j.apsusc.2022.156045

Chaudhary, V. and Nehra, S. P., Pt-sensitized MoO_3/mpg-CN mesoporous nanohybrid: A highly sensitive VOC sensor, *Microporous Mesoporous Mater.,* 315, 110906 (2021). https://doi.org/10.1016/j.micromeso.2021.110906

Chaudhuri, S. K., Kleppinger, J. W., Karadavut, O. F., Nag, R., Panta, R., Agostinelli, F., Sheth, A., Roy, U. N., James, R. B. and Mandal, K. C., Synthesis of CdZnTeSe single crystals for room temperature radiation detector fabrication: mitigation of hole trapping effects using a convolutional neural network, *J. Mater. Sci. Mater. Electron.,* 33(3), 1452–1463 (2022). https://doi.org/10.1007/s10854-021-07623-6

Chen, K., Jiang, Y., Tao, W., Wang, T., Liu, F., Wang, C., Yan, X., Lu, G. and Sun, P., MOF Structure engineering to synthesize core-shell heterostructures with controllable shell layer thickness: Regulating gas selectivity and sensitivity, *Sens. Actuat. B: Chem.,* 378, 133117 (2023). https://doi.org/10.1016/j.snb.2022.133117

Fang, J., Ma, Z. H., Xue, J. J., Chen, X., Xiao, R. P. and Song, J. M., Au doped In_2O_3 nanoparticles: Preparation, and their ethanol detection with high performance, *Mater. Sci. Semiconduct. Proce.,* 146, 106701 (2022). https://doi.org/10.1016/j.mssp.2022.106701

Ganvir, H. V, Kumar, S., Kumar, R., Haldar, B., Palanisamy, S., Verma, R., Dolas, D. R., Arun, V., Jadhav, V. D. and Selvaraju, M., Monitoring Atomic Layer Deposition by Potentiodynamic Electrochemical Impedance Spectroscopy of Multielement Adlayers, *J. New Mater. Electrochem. Syst.,* 27(3), 172–181 (2024). https://doi.org/10.14447/jnmes.v27i3.a02

Girimurugan, R., Selvaraju, P., Jeevanandam, P., Vadivukarassi, M., Subhashini, S., Selvam, N., Ahammad, S. K. H., Mayakannan, S. and Vaithilingam, S. K., Application of Deep Learning to the Prediction of Solar Irradiance through Missing Data, *Int. J. Photoenergy,* 2023, 1-17 (2023). https://doi.org/10.1155/2023/4717110

Sim, L. C., Tai, J. Y., Leong, K. H., Saravanan, P., Tan, S. T., Chong, W. C., & Aziz, A. A., Metal free and sunlight driven g-C3N4 based photocatalyst using carbon quantum dots from Arabian dates: Green strategy for photodegradation of 2,4-dichlorophenol and selective detection of Fe^{3+}. *Diamond and Related Materials*, 120, 108679. (2021). https://doi.org/https://doi.org/10.1016/j.diamond.2021.108679

Han, C., Li, X., Liu, J., Dong, H., Cheng, W., Liu, Y., Xin, J., Li, X., Shao, C. and Liu, Y., In_2O_3/g-C_3N_4/Au ternary heterojunction-integrated surface plasmonic and charge-separated effects for room-temperature ultrasensitive NO_2 detection, *Sens. Actuat. B: Chem.*, 371, 132448 (2022). https://doi.org/10.1016/j.snb.2022.132448

Han, C., Li, X., Liu, Y., Tang, Y., Liu, M., Li, X., Shao, C., Ma, J. and Liu, Y., Flexible All-Inorganic Room-Temperature Chemiresistors Based on Fibrous Ceramic Substrate and Visible-Light-Powered Semiconductor Sensing Layer, *Adv. Sci.,* 8(23), 2102471 (2021). https://doi.org/10.1002/advs.202102471

Henriquez, D. V. D. O., Kang, M., Cho, I., Choi, J., Park, J., Gul, O., Ahn, J., Lee, D. S. and Park, I., Low-Power, Multi-Transduction Nanosensor Array for Accurate Sensing of Flammable and Toxic Gases, *Small Meth*., 7(3), 2201352 (2023). https://doi.org/10.1002/smtd.202201352

Jasim, M. N. and Sameer, A. K., Tunable Optical and Sensing Properties of CdO and CdO-In_2O_3 thin Films for NH_3 Detection, *J. Environ. Nanotechnol.,* 13(4), 546–552 (2024). https://doi.org/10.13074/jent.2024.12.243936

Jin, Z., Wang, C., Wu, L., Liu, H., Shi, F., Zhao, J., Liu, F., Fu, K., Wang, F., Wang, Z. and Liu, J., *Physicochem. Eng. Aspects.,* 659, 130738 (2023). https://doi.org/10.1016/j.colsurfa.2022.130738

Kogularasu, S., Sriram, B., Wang, S. F. and Sheu, J. K., Sea-Urchin-Like Bi_2S_3Microstructures Decorated with Graphitic Carbon Nitride Nanosheets for Use in Food Preservation, *ACS Appl. Nano Mater.,* 5(2), 2375–2384 (2022). https://doi.org/10.1021/acsanm.1c04055

Kulkarni, S. and Ghosh, R., CuO–ZnO p-n junctions for accurate prediction of multiple volatile organic compounds aided by machine learning algorithms, *Anal. Chimica Acta.,* 1253, 341084 (2023). https://doi.org/10.1016/j.aca.2023.341084

Kumari, P., Kumar, R., Kumar, A. and Singh, R. K., Nanosensors for Monitoring and Detecting Nanoparticle Effects on Crops, *J. Environ. Nanotechnol.,* 14(1), 37–51 (2025). https://doi.org/10.13074/jent.2025.03.2511272

Liu, J., Liu, Y., Liu, H., Pan, Q. and Zhang, G., Construction of MOF-derived In_2O_3/g-C_3N_4/rGO nanostructures to enhance NO_x gas-sensitive properties at room temperature, *Sens, Actuat. B: Chem.*, 380, 133308 (2023). https://doi.org/10.1016/j.snb.2023.133308

Liu, X., Zhang, L., Li, Y., Xu, X., Du, Y., Jiang, Y. and Lin, K., A novel heterostructure coupling MOF-derived fluffy porous indium oxide with g-C_3N_4 for enhanced photocatalytic activity, *Mater. Res. Bullet.,* 133, 111078 (2021). https://doi.org/10.1016/j.materresbull.2020.111078

Liu, Y., Liu, J., Pan, Q., Pan, K. and Zhang, G., Metal-organic framework (MOF) derived In_2O_3 and g-C_3N_4 composite for superior NOx gas-sensing performance at room temperature, *Sens. Actuat. B: Chem.*, 352, 131001 (2022). https://doi.org/10.1016/j.snb.2021.131001

Nehru, R., Chen, C.-W., & Dong, C.-D., In-situ growth of MoS2 nanosheets on g-C3N4 nanotube: A novel electrochemical sensing platform for vanillin determination in food samples. *Carbon*, 208, 410–420.(2023). https://doi.org/https://doi.org/10.1016/j.carbon.2023.03.053

Samuel, B. E., Alghamdi, S., Priya, T., Deepalakshmi, R., Kannan, S. and Selvaraju, M., Deep Learning-Driven Culvert Monitoring: A Novel Approach for Flash Flood Mitigation through Visual Blockage Analysis, *IEEE 9th Int. Conf. Converg. Technol.,* 1-7 (2024). https://doi.org/10.1109/I2CT61223.2024.10543968

Selamneni, V., Gohel, K., Bokka, N., Sharma, S. and Sahatiya, P. MoS_2-Based Multifunctional Sensor for Both Chemical and Physical Stimuli and Their Classification Using Machine Learning Algorithms, *IEEE Sens. J.,* 21(3), 3694–3701 (2021). https://doi.org/10.1109/JSEN.2020.3023309

Shanavash, A., Sri, T. S., Mayakannan, S., Shanmugam, S. K., Chandankhede, P. H. and Sivakumar, B. G., Development of a carbon–perovskite self-powered IoT sensor node with dual-mode sensing, *Interact*., 247(1), 175 (2026). https://doi.org/10.1007/s10751-026-02516-8

Van, T. P., Hoang, M. L., Van, D. N. and Manh, H. C. Porous In_2O_3 nanorods fabricated by hydrothermal method for an effective CO gas sensor, *Mater. Res. Bullet.,* 137, 111179 (2021). https://doi.org/10.1016/j.materresbull.2020.111179

Wankhade, V. D. and Pedhekar, R. B., Fe-incorporated ZnO-TiO_2 Nanocomposites for Improved CO_2 Sensing, *J. Environ. Nanotechnol.,* 14(2), 129–138 (2025). https://doi.org/10.13074/jent.2025.06.2511430

Wu, X., Wang, H., Wang, J., Chen, J., Shi, L., Han, B. and Tian, X., Hydrothermal synthesis of flower-like Cr_2O_3-doped In_2O_3 nanorods clusters for ultra-low isoprene detection, *Colloids Surf. A: Physicochem. Eng. Aspects,* 620, 126606 (2021). https://doi.org/10.1016/j.colsurfa.2021.126606

Xu, M., Zhao, X., Jiang, H., Chen, S. and Huo, P., MOFs-derived C-In_2O_3/g-C_3N_4 heterojunction for enhanced photoreduction CO_2, *J. Environ. Chem. Eng.,* 9(6), 106469 (2021). https://doi.org/10.1016/j.jece.2021.106469

Yang, W., Chen, H. and Lu, J., Assembly of stacked In_2O_3 nanosheets for detecting trace NO_2 with ultrahigh selectivity and promoted recovery, *Appl. Surf. Sci.,* 539, 148217 (2021). https://doi.org/10.1016/j.apsusc.2020.148217